THE JOURNAL OF PHYSICAL CHEMISTRY C

pubs.acs.org/JPCC Article

Insight into Crystal Phase Dependent CO Dissociation on Rh Catalyst from DFT and Microkinetic Modeling

Xiaobin Hao, Riguang Zhang,* Lixia Ling, Maohong Fan, Debao Li, and Baojun Wang*

Cite This: J. Phys. Chem. C 2020, 124, 6756−6769 Read Online

ACCESS | Metrics & More | Article Recommendations | Supporting Information

ABSTRACT: For the sake of understanding deeply the formation of the ethanol from CO hydrogenation on the rhodium-based catalyst, the investigation on the relationship of the activity−structure for CO dissociation on Rh metal surface is necessary. Here, the effect of FCC and HCP Rh crystal phases and Rh surfaces on CO dissociation is predicted through DFT calculations, the equilibrium crystal shapes, and microkinetic modeling. The calculated overall activation barriers show that the H-assisted pathway with the relatively lower barrier energies is favorable compared with the direct one, which is independent of Rh crystal phases and surfaces. Among different FCC and HCP Rh surfaces, the (100) surface exhibits the highest CO dissociation activity with the relative reaction rate of 1.28×10^{11}, which is at least 10^5 times those on other surfaces. The CO dissociation activity of FCC Rh depends on (100) and (111) while that of HCP Rh depends on (0001), (10−12), and (10−10). The CO conversion rate on FCC Rh is about 10^4 times that on HCP Rh, suggesting that FCC Rh has a higher activity than HCP Rh. Moreover, the quantitative study shows that CO dissociation is primarily dependent on the electronic effect on Rh surfaces by the barrier decomposition method. PDOS, COHP, differential charge density, and Mulliken and Loewdin charges were further analyzed. Finally, this study can be expected to enrich the knowledge of the activity−structure of CO dissociation on Rh catalyst and provide a valuable guide for designing efficient Rh catalyst to improve CO conversion.

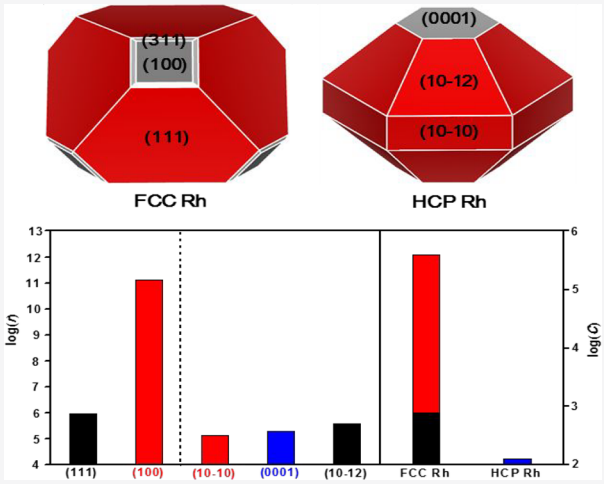

1. INTRODUCTION

The hydrogenation of carbon monoxide to ethanol on a metal-based catalyst becomes a promising reaction.[1−6] Three stages have been proposed in the reaction: (1) CO dissociation, including the direct and H-assisted pathway, followed by hydrogenation to the key intermediate CH_x species; (2) CO/CHO insertion into the intermediate CH_x to produce $CH_xC(H)O$; (3) $CH_xC(H)O$ hydrogenation to ethanol.[7] Thus, as an initial stage, CO dissociation is an important step for the formation of the key intermediates CH_x and ethanol and often considered as the rate-controlling step.[8,9]

CO dissociation depends largely on the crystal shape of metal material.[10−14] The hexagonal close-packed (HCP) and face-centered cubic (FCC) crystal phases exist for the metals Co, Ni, and Ru.[15−23] Experiments combining with density functional theory (DFT) showed that HCP Co possesses much better CO dissociation activity than FCC Co since the denser active sites can be available on HCP Co instead of FCC.[21] However, FCC Ni showed better activity of CO dissociation than HCP Ni due to more abundant active surfaces on FCC Ni.[22] Meanwhile, it is reported that a CO conversion rate over FCC Ru is ∼3 times higher than that over HCP Ru.[23] Therefore, the effect of crystal shape on CO dissociation is of importance for designing a highly efficient catalyst.

The metal Rh has been known as a promising element toward the formation of ethanol from CO hydrogenation.[8,9,24,25] The Rh catalyst with FCC crystal phase structure has been studied widely in both experiment and theory. The experimentally prepared Rh-based catalysts with FCC crystal phase exhibit a high selectivity of C_{2+} oxygenates but a low CO conversion.[27,28] Numerous DFT studies have been focused on CO dissociation on FCC Rh surfaces.[29−34] The results showed that the H-assisted pathway through CHO is the underlying activation way on Rh surfaces, and the studies also indicated that the stepped surfaces have higher activity than the flat surfaces.[30−33] However, CO dissociation on HCP Rh has rarely been studied, although the other metal nanoparticle with

Received: February 1, 2020
Revised: February 22, 2020
Published: March 4, 2020

https://dx.doi.org/10.1021/acs.jpcc.0c00909
J. Phys. Chem. C 2020, 124, 6756−6769

HCP crystal phase was reported to show different catalytic properties compared to FCC crystal phase.[15−23] Recent studies by Huang et al.[26] have successfully synthesized HCP Rh crystal phase by the experimental technology for the first time. As a result, the metal Rh can exist in the form of HCP and FCC crystal phase. However, the catalytic activity of CO dissociation on the newly synthesized HCP Rh remains unclear, and whether the HCP Rh can increase CO conversion and further improve the catalytic performance needs to be studied. Therefore, it is necessary to study CO dissociation on FCC and HCP Rh.

In this work, CO dissociation on two kinds of Rh crystal shapes (FCC and HCP) has been studied through combining the DFT method with the microkinetic modeling. Here, CO dissociation pathways, involving the direct pathway (CO → C + O) and H-assisted pathway through CHO and COH (CO + H → CHO → CH + O and CO + H → COH → C + OH), have been calculated on different surfaces of FCC and HCP Rh. Then, the structure sensitivity of CO dissociation pathways on Rh catalyst was discussed. In addition, based on two equilibrium shapes of FCC and HCP Rh, the activity difference of CO dissociation between FCC and HCP Rh crystal phase has been revealed. Moreover, the electronic and geometrical effects of Rh crystal phases on CO dissociation were illustrated.

2. CALCULATION DETAILS

2.1. Method and Model. All DFT calculations were performed by the projector-augmented wave (PAW) method in the Vienna Ab Initio Simulation Package (VASP).[35,36] The generalized gradient approximation (GGA) with a Perdew−Burke−Ernzerhof (PBE) formalism was applied.[37,38] The functional can produce rather accurate adsorption geometries and vibrational frequencies,[39] which is very well applicable in studying the heterogeneous catalytic reactions on metal catalyst so far.[40−45] Moreover, we have taken CO adsorption on Rh(111) as an example and compared the revised PBE and PBE-D3 functional with PBE functional (see Table S1); the results show that the PBE-D3 functional overestimates the CO adsorption energy compared with the PBE functional (−2.18 vs −1.96 eV). The revised PBE functional can give a lower adsorption energy (−1.66 eV) than the PBE and PBE-D3 functionals (−2.18 and −1.96 eV), which is close to the experimental value (−1.65 eV); however, the functional has the defect that worsens the descriptions of bulk crystals and surfaces[46−48] and will result in the higher barrier than PBE functional by Wang's report.[40] The cutoff energy was set to 400 eV. For structure optimization, the force on each atom and the energy difference were converged to 0.01 eV/Å and 5×10^{-6} eV. A k-point grid of $9 \times 9 \times 9$ was chosen to calculate the lattice parameters of FCC and HCP Rh bulk.

For the FCC Rh bulk, the calculated equilibrium lattice parameter is 3.839 Å, which accords with the reported values of 3.880 and 3.829 Å in experiment and theory, respectively.[26] For HCP Rh bulk, the calculated lattice parameters a and b are 2.730 Å and c is 4.407 Å, which accord with the experimental results (2.780 and 4.640 Å) and theoretical results (2.722 and 4.386 Å), respectively.[26] Subsequently, FCC Rh surfaces including the (111), (100), (110), (211), (221), and (311, and HCP Rh surfaces including the (0001), (10−10), (11−20), and (10−12), have been considered. For the surface size, the (111), (100), (110), and (0001) surface uses the $p(3 \times 3)$ supercells, while the $p(2 \times 3)$ supercells are used for (211), (221), (311), (10−10), (11−20), and (10−12) surfaces. The periodic slabs within 4−16 layers are used to model the different Rh surfaces, where the bottom 2 or 3 layers are fixed at the bulk position, while the remaining layers and the adsorbates are allowed to relax. The vacuum thickness of 10 Å is employed to avoid the interactions between the neighboring slabs. The surface structures and the different kinds of adsorption sites are shown in Figure S1.

In the calculation, considering that the surface species prefer to adsorb at the most stable site in the real situation, the most stable adsorption structures of surface species were used as the initial states for reactant and the final states for product.[21,22,33] The transition state structure was located through the Climbing-Image Nudged Elastic Band method (CI-NEB) and further optimized through the dimer method until the forces on atom become converged to 0.03 eV/Å.[49,50] The frequency analysis was performed to confirm only one imaginary frequency. To analyze the strength of the chemical bond, the Lobster package[51] with the wxDragon visualization tool[52] was used for the crystal orbital Hamilton population (COHP) and the atom-projected density of states (PDOS). The basis function 1s for the H element, 2s and 2p for C and O elements, and 5s, 5p, and 4d for the Rh element were employed. C−O, Ru−C, and Ru−O pair interactions within a distance 1.8−3.8 Å were considered for COHP calculation. In addition, the differential charge density and Mulliken and Loewdin charges were also analyzed.

The adsorption energy (E_{ads}) is calculated by the following formula:

$$E_{ads} = E_{adsorbate/surface} - E_{surface} - E_{adsorbate} \quad (1)$$

where $E_{adsorbate/surface}$, $E_{surface}$, and $E_{adsorbate}$ are the total energies of the Rh surface with the adsorbates, the clean Rh surface, and the adsorbate in the gaseous state, respectively.

The activation barrier (E_a) and reaction energy (ΔE) are calculated by the formulas

$$E_a = E_{TS} - E_{IS} \text{ and } \Delta E = E_{FS} - E_{IS} \quad (2)$$

where E_{IS}, E_{FS}, and E_{TS} correspond to the total energies of the initial states, final states, and transition states, respectively.

2.2. Surface Energy. According to Wulff's theory,[53] the equilibrium shape of FCC and HCP Rh can be constructed based on the different Rh surface energies. The bulk energy is important to obtain the accurate surface energy and equilibrium crystal shape.[54−57] Thus, to obtain FCC and HCP Rh bulk energy, a series of Rh(111) and (0001) surfaces with different layers are first calculated based on the following formula:

$$E_{sur}^{N} \approx 2A\gamma + NE_{bulk}^{crystal} \quad (3)$$

where E_{sur}^{N} is the energy of the surface with N layers, $2A$ is the total area of the top and bottom surface, γ is the surface energy, and N is the atomic number. $E_{bulk}^{crystal}$ is the energy of the bulk, which is calculated by makes an linear fit to the total energy of the surface as a function of the layer number and taking the slope.[57] The bulk energy $E_{bulk}^{crystal}$ of FCC and HCP Rh (E_{bulk}^{FCC} and E_{bulk}^{HCP}) can be obtained in Figure S2.

In addition, we construct different Rh surface models with $p(1 \times 1)$ and the thickness of at least 30 Å. The k-points of $9 \times 9 \times 1$ were used to optimize the surface models, where all Rh atoms are relaxed. The surface energy γ_{hkl} is determined by the formula of $\gamma_{hkl} = (E_{hkl} - NE_{bulk}^{crystal})/2A$, where E_{hkl} is the total energy of different Rh surfaces.

https://dx.doi.org/10.1021/acs.jpcc.0c00909
J. Phys. Chem. C 2020, 124, 6756−6769

2.3. Microkinetic Modeling. To quantify the dissociation rate on different FCC and HCP Rh surfaces, the elementary steps for three pathways of CO dissociation are assumed to be as follows. Moreover, the microkinetic modeling (see details in the Supporting Information) is applied based on the following elementary steps:

(1) For CO direct dissociation

$$CO + * \overset{K_1}{\leftrightarrow} CO* \tag{4}$$

$$CO* + * \overset{k_2}{\rightarrow} C* + O* \tag{5}$$

The rate of CO direct dissociation is defined via the following equation:

$$r_{dis} = k_2 \frac{P_{CO}K_1}{(P_{CO}K_1 + 1)^2} \tag{6}$$

(2) For H-assisted CO dissociation

$$CO + * \overset{K_1}{\leftrightarrow} CO* \tag{7}$$

$$H_2 + 2* \overset{K_2}{\leftrightarrow} 2H* \tag{8}$$

$$CO* + H* \underset{k_{-3}}{\overset{k_3}{\rightleftarrows}} COH* + * \text{ or } CO* + H* \underset{k_{-3}}{\overset{k_3}{\rightleftarrows}} CHO* + * \tag{9}$$

$$COH* + * \overset{k_4}{\rightarrow} C* + OH* \text{ or } CHO* + * \overset{k_4}{\rightarrow} CH* + O* \tag{10}$$

where the coverage of the intermediate (CHO and COH) is relatively steady with time according to the steady-state approximation. The reaction rate for H-assisted CO dissociation is defined via the following equation:

$$r_{dis} = \frac{k_3k_4}{k_{-3} + k_4} \times \frac{P_{CO}K_1{P_{H_2}}^{1/2}K_2^{1/2}}{\left(P_{CO}K_1 + {P_{H_2}}^{1/2}K_2^{1/2} + \frac{k_3}{k_4 + k_{-3}}P_{CO}K_1{P_{H_2}}^{1/2}K_2^{1/2} + 1\right)^2} \tag{11}$$

In addition, the total surface area of FCC or HCP Rh crystal shape is assumed to 1 m^2 for convenience, and all active sites can be used to activate CO molecules; the conversion rate (C) on the specified surface can be given by the following equation:[21]

$$C = r_{dis}N_{act} \tag{12}$$

where N_{act} is the number of the active sites, and can be obtained as the total surface area of the specified surface divided by the surface area per site.

3. RESULTS AND DISCUSSION

3.1. Equilibrium Shape of FCC and HCP Rh. Based on the calculated surface energy of different Rh surface models, the equilibrium shape of FCC and HCP Rh, the exposed surface area, and the occupied ratio are presented in Table 1 and Figure 1.

The FCC Rh crystal phase, as shown in Figure 1a, seems like an octahedron. It contains three exposed surfaces: (111), (311), and (100). As listed in Table 1, the (111) surface owns the lower surface energy (108 meV/Å^2) and occupies the most surface area ratio (88.1%). The (100) and (311) surfaces only occupy the small ratios of 7.5% and 4.4%, respectively. The other (221), (211), and (110) surfaces are missing in the equilibrium shape. The order of the occupied ratio for different FCC Rh surfaces is (111) > (100) > (311) > (221) = (211) = (110).

Table 1. Surface Energy (γ_{hkl}, meV/Å^2), Surface Area (S_a, Å^2), and the Corresponding Ratio (S_r, %) of the Different Rh Surfaces on FCC and HCP Rh Crystal Phase, Respectively

FCC Rh				HCP Rh			
surfaces	γ_{hkl}	S_a	S_r	surfaces	γ_{hkl}	S_a	S_r
(111)	108	49.56	88.1	(10−12)	123	47.16	68.8
(100)	141	4.22	7.5	(10−10)	153	14.18	20.7
(311)	140	2.48	4.4	(0001)	110	7.17	10.5
(110)	144	0	0	(11−20)	181	0	0
(211)	141	0	0				
(221)	136	0	0				

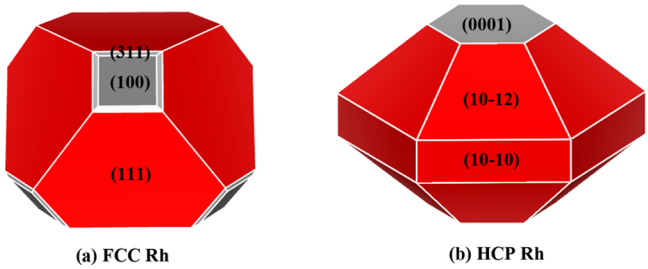

(a) FCC Rh (b) HCP Rh

Figure 1. Equilibrium shapes of FCC and HCP Rh crystal phases.

For HCP Rh crystal phase, as shown in Figure 1b, the equilibrium shape seems like an octadecahedron. It also contains three exposed surfaces: (10−12), (10−10), and (0001). As shown in Table 1, similar to the (111) surface, the (0001) owns the lower surface energy of 110 meV/Å^2 while covers only 10.5% in the equilibrium shape. On the contrary, the (10−12) and (10−10) surface with larger surface energy of 123 and 153 meV/Å^2 occupy the ratio of 68.8% and 20.7%, respectively, and the remaining (11−20) surface has the highest surface energy of 181 meV/Å^2 and disappears in the equilibrium shape. Therefore, on HCP Rh crystal phase, the order of the surface area ratio is (10−12) > (10−10) > (0001) > (11−20).

3.2. Adsorption of Reactant and Product. In the section, the adsorption energies of the various species (CO, C, O, H, CHO, COH, CH, and OH) involving the indirect and H-assisted pathway were calculated. The most stable adsorption site and adsorption energies are presented in Table S2. As shown in the table, although the adsorption sites of CO on different FCC and HCP Rh surfaces are different, the adsorption energies of CO are in the range of −1.87 to −2.02 eV on FCC Rh and −2.05 to −2.13 eV on HCP Rh, respectively, which suggest that CO adsorption is structure insensitive on the Rh catalyst. Similar to CO adsorption, the adsorption energy of H is between −2.66 and −2.83 eV, suggesting that H adsorption is also structure insensitive.

C and CH locate at the 3(4)-fold hollow site on different FCC and HCP Rh surfaces; namely, both of them prefer to coordinate with much more Rh atoms. This may be attributed to that the electron deficiency of C or CH is difficult to fulfill the octet rule. The change value of the adsorption energy of 0.83 and 0.67 eV suggests that C and CH adsorption are structure sensitive on Rh catalyst.

https://dx.doi.org/10.1021/acs.jpcc.0c00909
J. Phys. Chem. C 2020, 124, 6756−6769

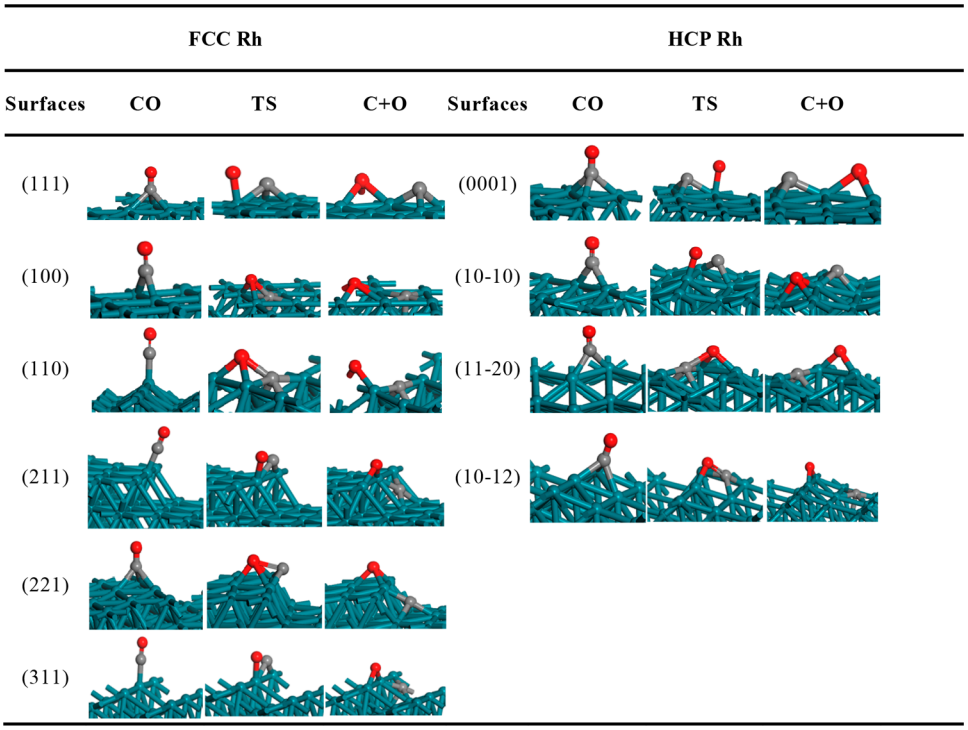

Figure 2. Optimized structures of CO, the coadsorbed C and O, and the transition state structure for CO direct dissociation on different FCC and HCP Rh surfaces. The C, O, and Rh atoms are shown in gray, red, and green colors, respectively.

The adsorption energy of O atom is in the range between −5.40 and −5.81 eV on different Rh surfaces, and the corresponding adsorption site is different. Compared with the O atom, the adsorbate of OH lacks one electron to fulfill the octet rule, and the bonded H atom reduces the coordination unsaturation of O atom. This keeps OH locating exclusively at the 2-fold bridge site with E_{ads} of −3.06 to −3.75 eV on different Rh surfaces. The change values of 0.41 and 0.69 eV in E_{ads} show that O and OH adsorption is structure sensitive on the Rh catalyst. To sum up, the adsorption of reactant CO and H is structure insensitive while that of products C, CH, O, and OH is structure sensitive to CO dissociation on the Rh catalyst.

3.3. CO Dissociation. *3.3.1. CO Direct Dissociation.* In this section, the direct pathway was calculated, where the structures of the initial state (IS) for the adsorbed CO, the transition state (TS), and the final state (FS) for the coadsorbed C and O are presented in Figure 2. The activation barrier, reaction energy, and the detailed structural parameters are presented in Table 2.

Table 2. Activation Barrier (E_a, eV), Reaction Energy (ΔE, eV), and the Distance between C and O Atoms in the Transition State Structure (d_{TS}, Å) for CO Direct Dissociation on Different FCC and HCP Rh Surfaces

FCC Rh				HCP Rh			
surfaces	E_a	ΔE	d_{TS}	surfaces	E_a	ΔE	d_{TS}
(111)	3.74	1.38	2.139	(0001)	3.55	1.06	2.177
(100)	2.14	0.61	1.909	(10−10)	3.84	1.41	2.237
(110)	2.17	0.99	1.883	(11−20)	2.80	1.60	1.952
(211)	4.15	0.77	2.011	(10−12)	2.67	1.38	1.835
(221)	3.49	0.80	1.945				
(311)	4.05	0.76	2.013				

On the FCC Rh, both (211) and (311) surfaces have the largest E_a of 4.15 and 4.05 eV and the positive ΔE of 0.77 and 0.76 eV, respectively. Both (100) and (110) surfaces exhibit the most activity with the least E_a of 2.14 and 2.17 eV as well as the ΔE of 0.61 and 0.99 eV, respectively. The remaining (111) and (221) surfaces have the modest E_a of 3.74 and 3.49 eV, respectively, and the corresponding ΔE is 1.38 and 0.80 eV, respectively. For the HCP Rh, the (10−12) and (11−20) surfaces are the most active surfaces with the least E_a (2.67 and 2.80 eV), and this corresponding ΔE is positive (1.38 and 1.60 eV), followed by the (0001) and (10−10) surfaces, where the calculated E_a and ΔE are 3.55 and 1.06 eV, as well as 3.84 and 1.41 eV, respectively. Therefore, the E_a changes from 2.14 to 4.15 eV and from 2.67 to 3.85 eV on FCC and HCP Rh, respectively.

To summarize, the larger change values in E_a suggest that the direct pathway is highly sensitive to Rh surface structures and crystal phases, which accords with the studies of Li et al. on Co and Ni.[21,22] The least E_a are 2.14 and 2.17 eV on the (100) and (110) surface for FCC Rh as well as 2.64 and 2.80 eV on the (10−12) and (11−20) surface for HCP Rh. The difference in the least activation barriers between FCC and HCP Rh surfaces suggests that FCC Rh might have higher CO direct dissociation activity than HCP Rh in case the (100), (110), (10−12), and (11−20) surfaces can be available and cover the similar area ratios on their respective crystal phase. In addition, the least E_a of 2.14 eV on the Rh catalyst is larger by 1.74 and 1.07 eV than that on the Ni and Co catalysts for CO direct dissociation, respectively,[21,22] which suggests that CO direct dissociation activity on the Rh catalyst is low compared to that on the Ni and Co catalysts. Meanwhile, the pathway is highly endothermic, which is irrespective of Rh surface structure and crystal phase.

https://dx.doi.org/10.1021/acs.jpcc.0c00909
J. Phys. Chem. C 2020, 124, 6756−6769

Table 3. The (Overall) Activation Barrier ($E_{a,1}$, $E_{a,2}$, and E_a, eV), Reaction Energy (ΔE_1, ΔE_2, and ΔE, eV), and the Distance ($d_{TS,1}$ and $d_{TS,2}$, Å) of the Forming C−H and Breaking C−O in the Transition State Structure for H-Assisted CO Dissociation via the CHO Intermediate on Different FCC and HCP Rh Surfaces, Respectively

	CO + H → CHO			CHO → CH + O			CO + H → CH + O	
surfaces	$E_{a,1}$	ΔE_1	$d_{TS,1}$	$E_{a,2}$	ΔE_2	$d_{TS,2}$	E_a	ΔE
				FCC Rh				
(111)	1.52	1.03	1.183	1.41	−0.17	1.835	2.44	0.86
(100)	1.31	0.61	1.360	1.85	−0.09	2.035	2.46	0.52
(110)	0.90	0.56	1.183	1.71	0.46	1.919	2.27	1.02
(211)	1.25	0.84	1.182	3.13	0.14	2.019	3.97	0.98
(221)	1.26	0.85	1.169	3.02	0.17	2.686	3.87	1.02
(311)	1.24	0.84	1.181	2.62	0.17	2.059	3.46	1.01
				HCP Rh				
(0001)	1.44	1.08	1.169	1.33	−0.34	1.853	2.41	0.74
(10−10)	1.53	0.87	1.192	1.94	0.39	1.820	2.81	1.26
(11−20)	1.33	0.85	1.182	2.03	0.29	1.908	2.88	1.14
(10−12)	1.20	0.83	1.170	1.49	0.05	1.855	2.32	0.88

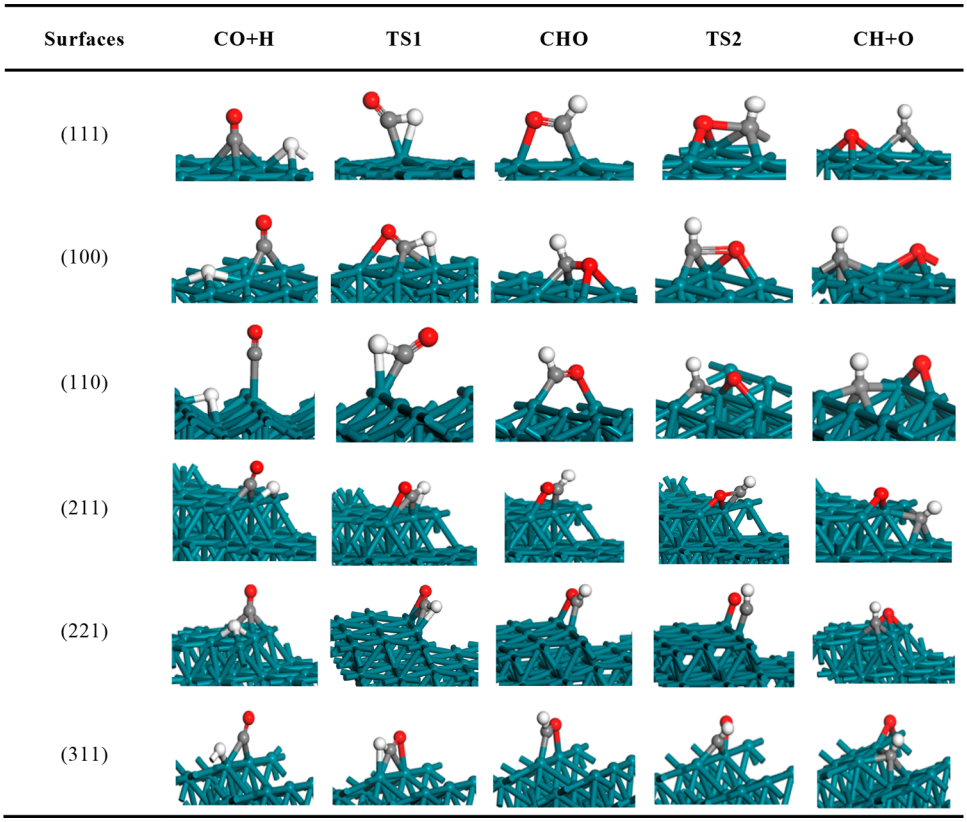

Figure 3. Optimized structures of the coadsorbed CO and H, the intermediate CHO, the transition state structures (TS1 and TS2), and the coadsorbed CH and O for H-assisted CO dissociation to CH on different FCC Rh surfaces. The C, O, H, and Rh atoms are shown in the gray, red, white, and green colors, respectively.

3.3.2. H-Assisted CO Dissociation via the CHO Intermediate. H-assisted pathway via CHO can occur through the hydrogenation on C atom in adsorbed CO. In this section, the two successive elementary steps, CO + H → CHO and CHO → CH + O, were calculated. The corresponding activation barrier ($E_{a,1}$, $E_{a,2}$) and reaction energy (ΔE_1, ΔE_2) are presented in Table 3. The IS structures of the coadsorbed CO and H, the intermediates CHO, FS structures of the coadsorbed CH and O, and TS structures on different FCC and HCP Rh surfaces are presented in Figures 3 and 4.

For CO + H → CHO, the calculated $E_{a,1}$ range is 0.90−1.52 eV on FCC Rh and 1.20−1.53 eV on HCP Rh. The reaction energy ΔE_1 is exclusively endothermic, which is independent of the Rh surface structures and crystal phase. The corresponding ranges are 0.56−1.03 eV and 0.83−1.08 eV on FCC and HCP Rh, respectively. For CHO → CH + O, the calculated $E_{a,2}$ and ΔE_2 range are 1.41−3.13 eV and −0.17−0.46 eV on FCC Rh and 1.33−2.03 eV and −0.34−0.39 eV on HCP Rh, respectively. The $E_{a,2}$ and ΔE_2 change in value by 1.80 and 0.80 eV on all the surfaces, respectively, which are larger than the change value (0.63 and 0.52 eV) in $E_{a,1}$ and ΔE_1. Therefore, CHO dissociation is more structure sensitive than its formation in kinetics and thermodynamics.

https://dx.doi.org/10.1021/acs.jpcc.0c00909
J. Phys. Chem. C 2020, 124, 6756−6769

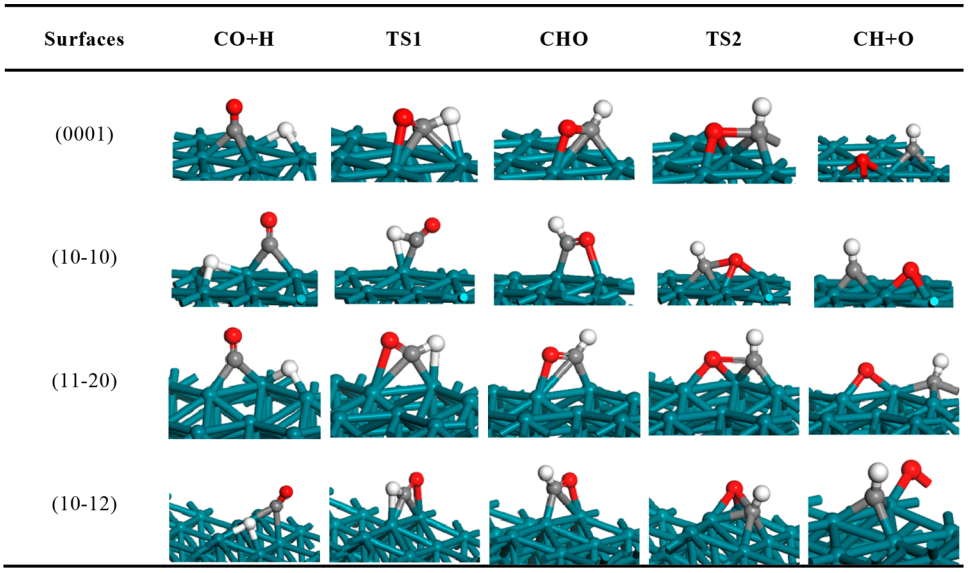

Figure 4. Optimized structures of the coadsorbed CO and H, the intermediate CHO, the transition state structures (TS1 and TS2), and the coadsorbed CH and O for H-assisted CO dissociation to CH on different HCP Rh surfaces. The C, O, H, and Rh atoms are shown in the gray, red, white, and green colors, respectively.

Table 4. The (Overall) Activation Barrier ($E_{a,1}$, $E_{a,2}$, and E_a, eV), Reaction Energy (ΔE_1, ΔE_2, and ΔE, eV), and the Distance ($d_{TS,1}$ and $d_{TS,2}$, Å) of the Forming O−H and Breaking C−O in the Transition State Structure for H-Assisted CO Dissociation via the COH Intermediate on Different FCC and HCP Rh Surfaces, Respectively

	CO + H → COH			COH → C + OH			CO + H → C + OH	
surfaces	$E_{a,1}$	ΔE_1	$d_{TS,1}$	$E_{a,2}$	ΔE_2	$d_{TS,2}$	E_a	ΔE
				FCC Rh				
(111)	1.69	0.61	1.331	1.91	0.98	2.146	2.52	1.59
(100)	1.66	0.52	1.381	1.38	−0.16	2.005	1.90	0.36
(110)	1.87	0.91	1.287	0.90	−0.31	2.004	1.87	0.58
(211)	2.02	1.07	1.272	2.16	−0.57	2.044	3.23	0.50
(221)	1.95	0.86	1.294	1.00	−0.57	2.042	1.95	0.29
(311)	2.00	0.89	1.267	2.23	−0.41	2.061	3.12	0.48
				HCP Rh				
(0001)	1.76	0.65	1.343	1.88	0.89	2.153	2.54	1.54
(10−10)	1.54	0.72	1.301	1.64	0.57	3.238	2.36	1.29
(11−20)	1.64	1.04	1.297	1.64	0.16	2.066	2.68	1.20
(10−12)	1.23	0.84	1.277	2.17	−0.15	1.817	3.01	0.69

The overall activation barriers (E_a) and reaction energies (ΔE) for CO + H → CH + O are presented in Table 3. As seen from Table 3, the E_a changes from 2.27 to 3.97 eV, and the corresponding change value is 1.70 eV. The structural sensitivity of H-assisted pathway via CHO is decreasing obviously in comparison with the direct one, in which the change value of E_a is 2.01 eV. The most active surfaces are (110) and (10−12) with the least E_a of 2.27 and 2.32 eV, followed by (0001), (111), and (100) with E_a of 2.41, 2.44, and 2.46 eV, respectively. (110), (100), and (10−12) remain the active surface, as also found in the direct pathway. Compared with direct dissociation pathway, the barriers of H-assisted pathway via CHO are 1.30 and 1.11 eV lower on the closed-packed (111) and (0001), respectively. For the remaining (211), (311), and (10−10) surfaces, the calculated activation barriers for H-assisted pathway via CHO are also lower than those for direct one. Therefore, H-assisted CO dissociation via CHO is favorable than direct dissociation as a whole.

3.3.3. H-Assisted CO Dissociation via the COH Intermediate. The H-assisted pathway via COH can occur through the hydrogenation on O atom in adsorbed CO. In this section, two successive elementary steps, CO + H → COH and COH → C + OH, were calculated. Correspondingly, the activation barrier ($E_{a,1}$, $E_{a,2}$) and the reaction energy (ΔE_1, ΔE_2) are listed in Table 4. The IS structures for the coadsorbed CO and H, the intermediates COH, the FS structures for the coadsorbed C and OH, and TS structures are presented in Figures 5 and 6.

For CO + H → COH, the calculated activation barriers, $E_{a,1}$, are in the range of 1.66−2.02 eV on FCC Rh and 1.23−1.76 eV on HCP Rh. Similar to CHO, COH formation is exclusively endothermic. The corresponding ΔE_1 range is 0.52−1.07 eV on FCC Rh and 0.65−1.04 eV on HCP Rh. For COH → C + OH, the calculated activation barriers, $E_{a,2}$, range from 0.90 to 2.23 eV on FCC Rh and from 1.64 to 2.17 eV on HCP Rh. The calculated ΔE_2 range is −0.57−0.98 eV on FCC Rh and −0.15−0.89 eV on HCP Rh. Therefore, COH dissociation is also more structure sensitive than its formation.

https://dx.doi.org/10.1021/acs.jpcc.0c00909
J. Phys. Chem. C 2020, 124, 6756−6769

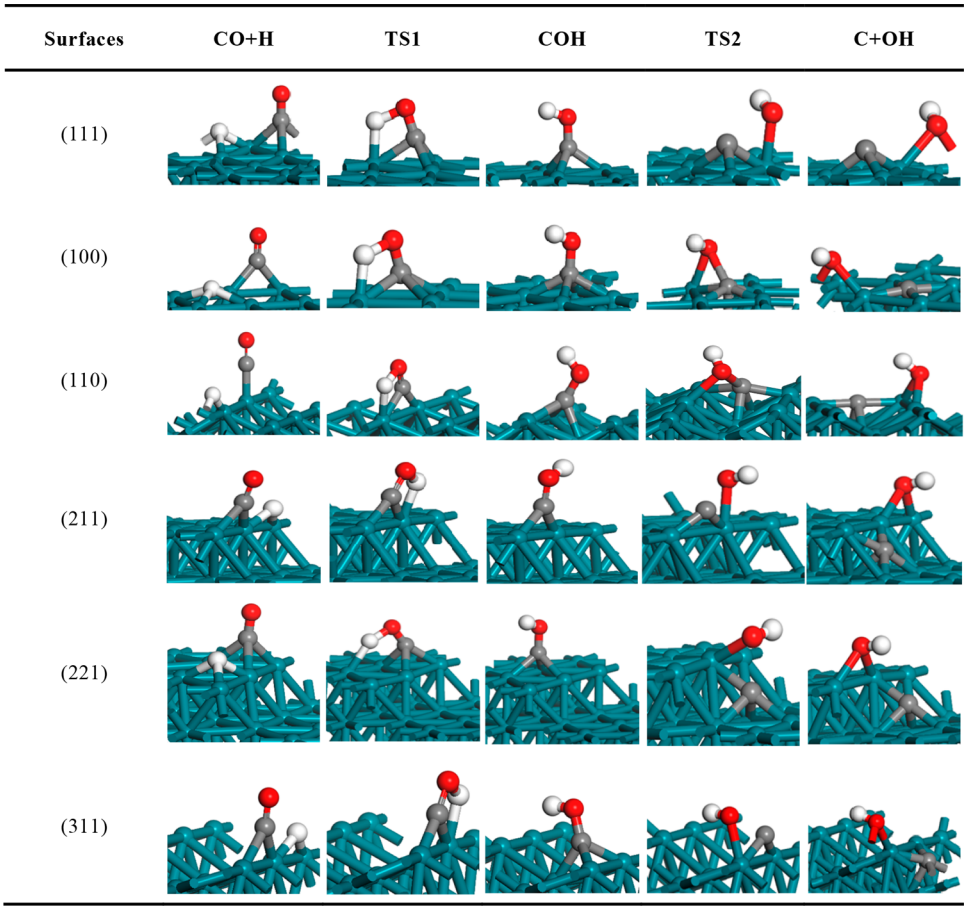

Figure 5. Optimized structures of the coadsorbed CO and H, the intermediate COH, the transition state structures (TS1 and TS2), and the coadsorbed C and OH for H-assisted CO dissociation to C on different FCC Rh surfaces. The C, O, H and Rh atoms are shown in gray, red, white, and green colors, respectively.

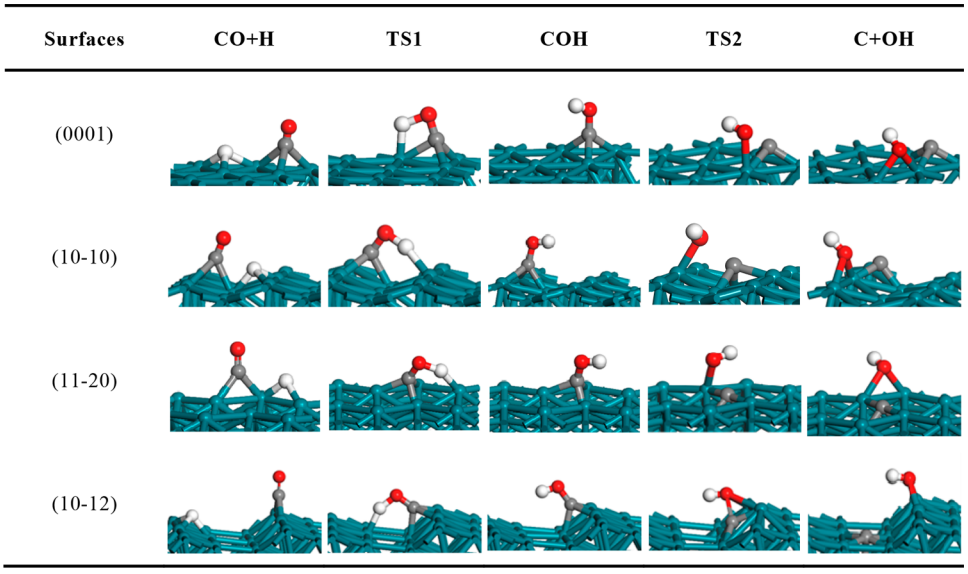

Figure 6. Optimized structures of the coadsorbed CO and H, the intermediate COH, the transition state structures (TS1 and TS2), and the coadsorbed C and OH for H-assisted CO dissociation to C on different HCP Rh surfaces. The C, O, H and Rh atoms are shown in gray, red, white, and green colors, respectively.

The breakage of C−O bond irrespective of CHO or COH needs less energy than that in CO.

In addition, as shown in Table 4, there are the least overall activation barriers of 1.87, 1.90, and 1.95 eV on (110), (100), and (221) surface, which are even lower than the least E_a on all Rh surfaces for the other two pathways, CO → C + O and CO + H → CH + O, calculated so far. Therefore, the (110), (100), and (221) are the most active surfaces for H-assisted pathway

https://dx.doi.org/10.1021/acs.jpcc.0c00909
J. Phys. Chem. C 2020, 124, 6756−6769

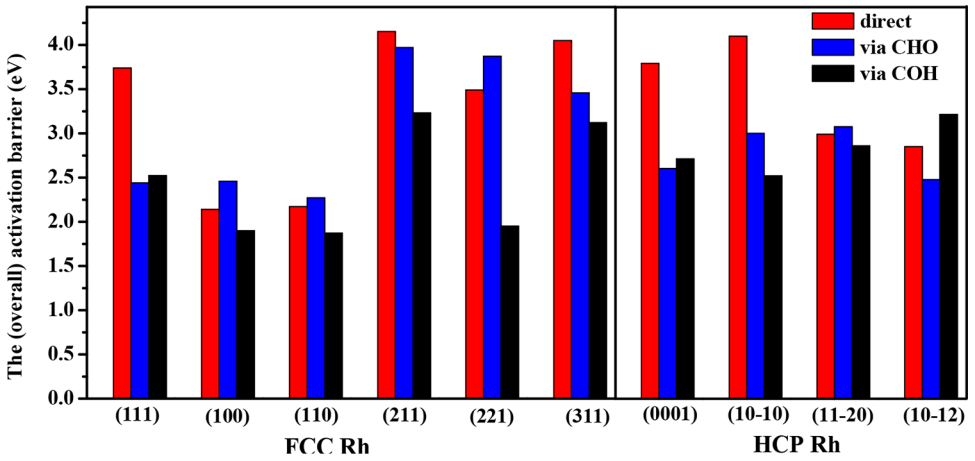

Figure 7. The (overall) activation barriers (eV) for CO direct dissociation (red) and H-assisted CO dissociation via the CHO (blue) and COH (black) intermediates on the FCC (left) and HCP (right) Rh crystal phase.

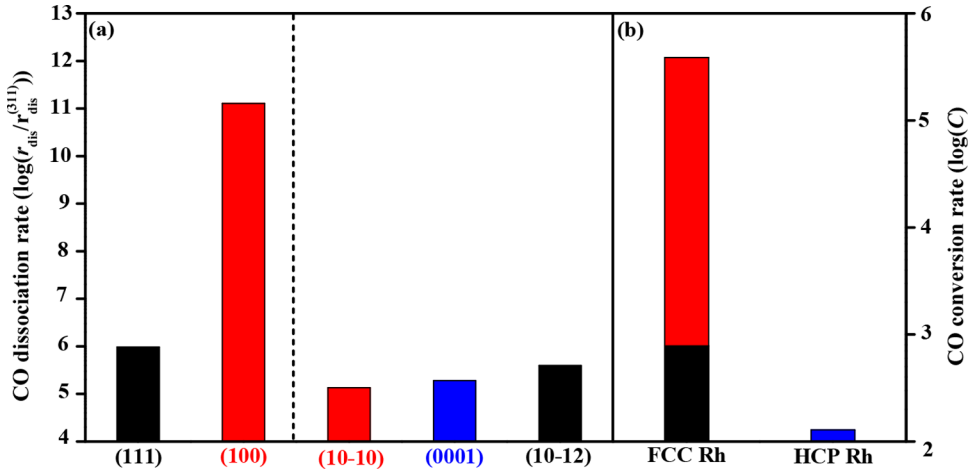

Figure 8. (a) CO dissociation rates (s^{-1} $site^{-1}$) on the exposed Rh surfaces. All rates are normalized by that of (311). (b) CO conversion rate (s^{-1}) on FCC (left) and HCP (right) Rh crystal phase at the temperature of 543 K, H_2/CO = 2, and H_2 partial pressure of 8 atm. The colors displayed in diagram (b) correspond to those in diagram (a) and represent the contribution of CO conversion rate of the different surfaces.

through COH. For the other surfaces, the calculated E_a range is 2.36−3.23 eV, and the change value of 1.36 eV on Rh surfaces indicates that H-assisted pathway via COH is highly structural sensitive. This may be ascribed to the structural sensitivity of the C adsorption from the dissociated COH.

3.4. FCC Rh vs HCP Rh. The overall barriers for the direct, H-assisted pathways through CHO and COH on different surfaces are presented in Figure 7. The H-assisted pathway on all Rh surfaces has a relatively lower barrier and is kinetically more advantageous than direct one on Rh catalyst. Thus, the presence of H_2 is beneficial for CO activation. Moreover, CO dissociation proceeds via the CHO intermediate on the (111), (0001), and (10−12) surface along with the barriers of 2.44, 2.41, and 2.32 eV, respectively. On the other surfaces, including the (100), (110), (211), (221), (311), (10−10), and (11−20), CO dissociation prefers to occur via CO + H → COH → C + OH with the overall activation barriers in the range from 1.87 to 3.23 eV.

CO dissociation rates on the exposed FCC and HCP surfaces have been first calculated by using the microkinetic modeling for purpose of comparing the activity of FCC and HCP Rh crystal phase. The relative dissociation rates at the reaction condition (P_{CO} = 4 atm, P_{CO}/P_{H_2} = 1/2, and T = 543 K) are presented in Figure 8a. The dissociation rate, rate constants, and surface coverage of intermediates are listed in Tables S3 and S4. The (311) surface has the smallest dissociation rate (1.03×10^{-21} s^{-1} $site^{-1}$), which is chosen as the reference to facilitate the comparison for the activity of different surfaces. Among six exposed surfaces, the (100) has the largest relative r of 1.28×10^{11}, followed by the (111), (10−12), (0001), and (10−10) with a similar r of 9.66×10^5, 3.94×10^5, 1.91×10^5, and 1.34×10^5, respectively. The predicted CO dissociation rate is extremely low due to the low surface coverage of CHO (COH) intermediates; as shown in Table S4, the order of surface coverage of the species is $\Theta_H > \Theta_{CO} > \Theta_{COH}$ (Θ_{CHO}). In addition, as seen from Table 1, the (100) and (111) surfaces with the occupied more than 90% of the surface area of FCC Rh crystal phase have larger dissociation rates than the (10−12), (0001), and (10−10) surfaces with the similar occupied ratio of HCP crystal phase, which suggests that FCC Rh crystal phase might have the higher activity than HCP one for CO dissociation.

In addition, to make a comparison between the activity of FCC and HCP Rh quantitatively, the CO conversion rates have been calculated based on the dissociation rates on the exposed surfaces in the equilibrium shape of FCC and HCP Rh

https://dx.doi.org/10.1021/acs.jpcc.0c00909
J. Phys. Chem. C 2020, 124, 6756−6769

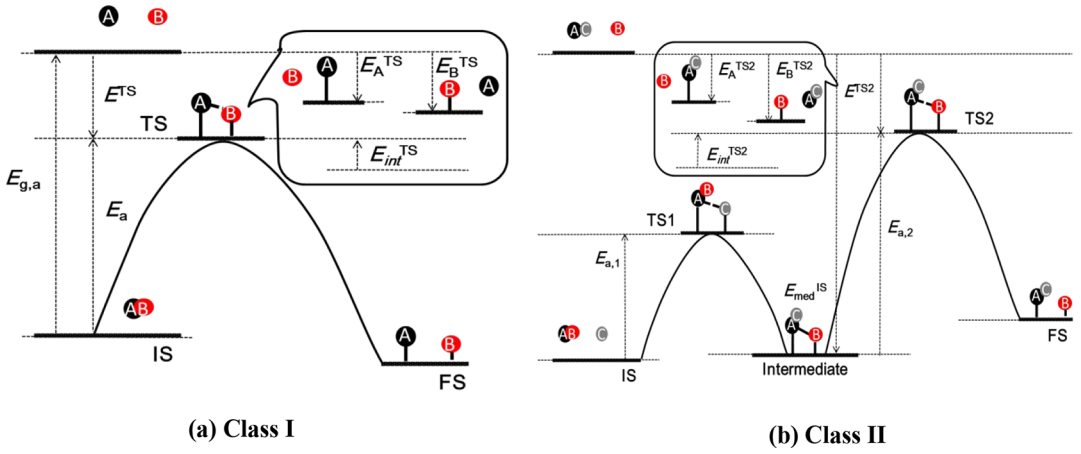

(a) Class I (b) Class II

Figure 9. Energetic diagrams for (a) Class I and (b) Class II. The inset shows the energy decomposition of the TS (E^{TS}) at TS. All of the terms are defined and discussed in the text.

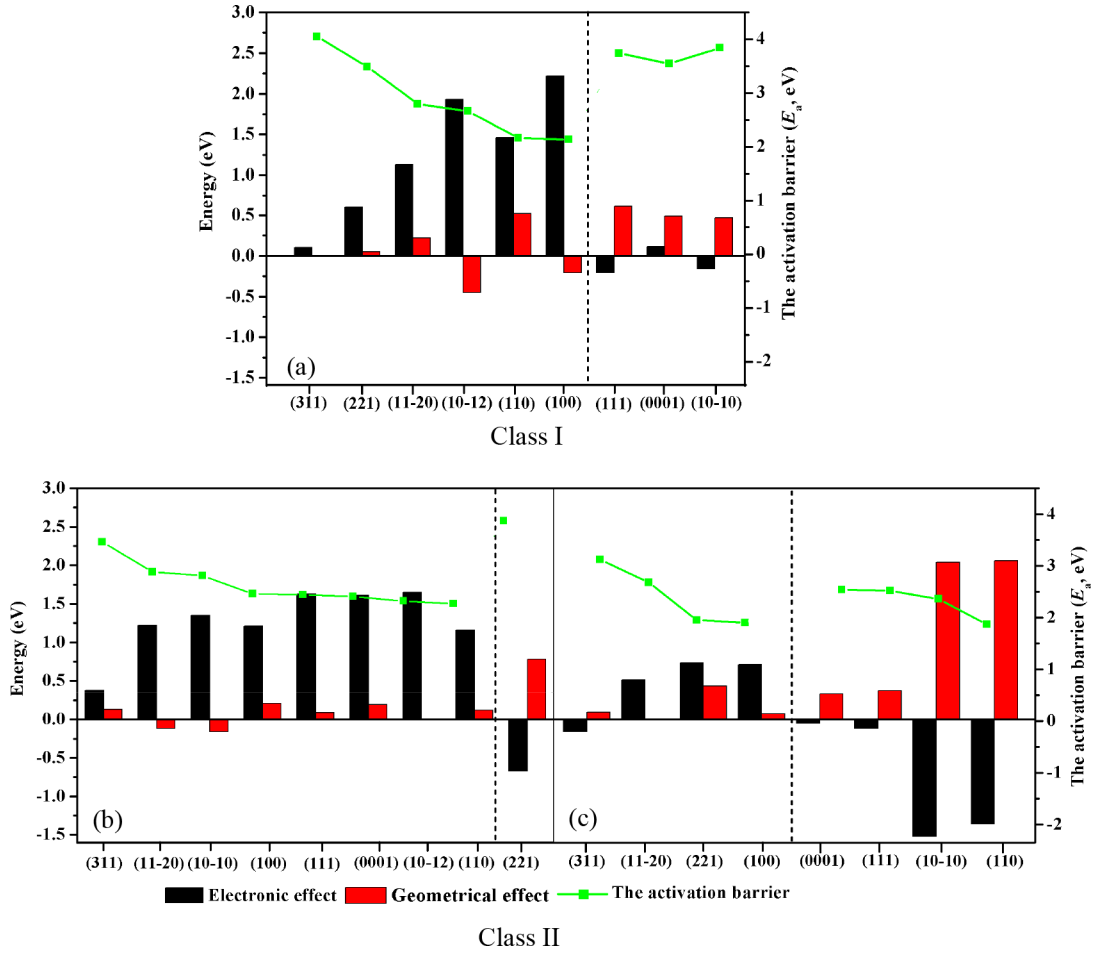

Figure 10. Electronic and geometrical effect for Class I and II on different Rh surfaces. The black and red bar show electronic and geometrical effect, respectively. The left and right areas of the dashed line represent the electronic and geometrical effect plays the key role, respectively. The inserted green line indicates the activation barriers for different CO dissociation pathways on different Rh surfaces. Note that the left and right of diagram (b) and (c) indicate H-assisted CO dissociation pathway via CHO and COH, respectively. All energies are normalized by that of (211) with units of eV.

and the corresponding area ratio. The CO conversion rates are presented in Figure 8b (see details in Table S5). For the FCC crystal phase, the CO dissociation rate on the (311) surface is smaller than those on other surfaces. Meanwhile, the (111) and (100) surfaces occupied more than 90% of the surface area of FCC Rh crystal phase; thus, the activity of the FCC Rh crystal phase depends on the (111) and (100) surface (see Figure 8b). In addition, the calculated CO conversion rate is 3.85×10^6 s^{-1} on the FCC Rh. For the HCP crystal phase, CO conversion rates correspond to 12.88, 36.35, and 78.43 s^{-1} on

https://dx.doi.org/10.1021/acs.jpcc.0c00909
J. Phys. Chem. C 2020, 124, 6756−6769

the (0001), (10−10), and (10−12) surfaces, which result in 1.28×10^2 s^{-1} of CO conversion rate on the HCP Rh. Thus, the CO conversion rate over the FCC Rh is larger by about 10^4 times than that over the HCP Rh; namely, the FCC Rh crystal phase has a higher activity than the HCP Rh crystal phase. In addition, the CO dissociation activity can be significantly improved when the occupied area ratio of the (100) surface increases on Rh catalyst (see Figure S3).

3.5. A Quantitative Method for the Electronic and Geometrical Effect. To understand CO dissociation in depth, the individual contributions of the electronic and geometrical effect to the activation barrier should be revealed.[58−60] The following barrier energy decomposition methods were utilized. Three CO dissociation pathways are classified into Class I and II in Figure 9. The CO → C + O reaction belongs to AB → A + B reaction, which is defined as Class I type. The H-assisted dissociation reaction belongs to the AB + C → ABC → AC + B reaction, which is defined as Class II type.

For Class I, as shown in Figure 9a, where the gaseous AB molecule dissociation to the adsorbed A and B atom on the catalyst, one can decompose the activation barrier, E_a, into three parts:

$$E_a = E_{g,a} + E^{TS} = E_{g,a} + (E_A{}^{TS} + E_B{}^{TS}) + E_{int}{}^{TS} \quad (13)$$

where $E_{g,a}$ is the gaseous AB bond energy and E^{TS} and $E_A{}^{TS}$ ($E_B{}^{TS}$) are the adsorption energy of TS and A (B) atom in TS without B (A) atom, respectively. $E_{int}{}^{TS}$ is the mutual interaction between A and B. In addition, for Class I reaction on different surfaces, to reflect the degree of the change in these parts intuitively, we can use one surface with the largest activation barrier as the reference standard according to ref 60:

$$E_a - E_a{}^{ref} = \Delta E_a = \Delta(E_A{}^{TS} + E_B{}^{TS}) + \Delta E_{int}{}^{TS} \quad (14)$$

The equation suggests that the difference of the barrier (ΔE_a) on different surfaces is caused by two parts: (i) $\Delta(E_A{}^{TS}, E_B{}^{TS})$, the negative value indicates that the electronic effect enhances the binding ability of A (B) on surface relative to the reference surface; and (ii) $\Delta E_{int}{}^{TS}$, the negative value shows that the geometrical effect weakens the repulsion between A and B atoms in TS. Moreover, the negative $\Delta(E_A{}^{TS}, E_B{}^{TS})$ and $\Delta E_{int}{}^{TS}$ suggest that the improved binding ability (the electronic effect) and weaken repulsion (the geometrical effect) can stabilize the TS and facilitate reducing the activation barrier.

For Class II, the second elementary step largely determines the overall process in H-assisted dissociation on surfaces (seen in Figure 9b); thus, we decompose the activation barrier, $E_{a,2}$, in the following equation:

$$E_{a,2} = E^{TS2} - E_{med}{}^{IS} = (E_{AC}{}^{TS} + E_B{}^{TS} + E_{int}{}^{TS}) - E_{med}{}^{IS} \quad (15)$$

where $E_{AC}{}^{TS}$, $E_B{}^{TS}$, and $E_{med}{}^{IS}$ are the adsorption energy of AC and B alone in TS and the ABC intermediate, respectively; $E_{int}{}^{TS}$ is the mutual interaction between AC and B. Similar to eq 14, the following equation can be obtained:

$$\Delta E_{a,2} = [\Delta(E_{AC}{}^{TS} + E_B{}^{TS}) + \Delta E_{int}{}^{TS}] - \Delta E_{med}{}^{IS} \quad (16)$$

The equation suggests that the difference of the barrier ($\Delta E_{a,2}$) on surfaces is caused by three parts: (i) $\Delta(E_{AC}{}^{TS}$ and $E_B{}^{TS})$, (ii) $\Delta E_{med}{}^{IS}$, and (iii) $\Delta E_{int}{}^{TS}$. The negative $\Delta(E_{AC}{}^{TS}$ and $E_B{}^{TS})$ and $\Delta E_{int}{}^{TS}$ decrease the barrier $E_{a,2}$; however, the negative $\Delta E_{med}{}^{IS}$ stabilizes the intermediate and increases the barrier $E_{a,2}$. Therefore, the electronic effect is reflected by the combination of $\Delta(E_{AC}{}^{TS}$ and $E_B{}^{TS})$ and $\Delta E_{med}{}^{IS}$, and the geometrical effect is reflected by $\Delta E_{int}{}^{TS}$.

In the following study, the (211) surface is thought as the reference standard, in which there are the highest (overall) activation barriers for three types of reactions. Figure 10 presents the electronic and geometrical effects for three dissociation pathways on different Rh surfaces (see Tables S6 and S7 for details). As can be seen from section 3.4, (100) exhibits the highest activity for CO dissociation, and meanwhile, there are the lower activation barriers for both of three dissociation pathways. Therefore, (100) is taken as an example below to clarify that how the surface structure affects CO dissociation and why the (100) surface exhibits so high activity.

(i) For Class I, as shown in Table S6, on the (100) surface, there is the large increase of 2.22 eV in $E_C{}^{TS}$ and $E_O{}^{TS}$ but the small $E_{int}{}^{TS}$ of 0.21 eV, which suggests that the electronic effect is obviously stronger than the geometrical effect (in Figure 10). The (100) surface has the strong binding ability of C and O atom and improves the TS stability significantly. Therefore, compared with the (211) surface, the reduction of E_a on the (100) surface is mainly caused by the electronic effect. In addition, as shown in Figure 10, the geometrical effect plays the more important role than the electronic effect on the (111), (0001), and (10−10) surface; however, the electronic effect plays the more important role on the (110), (221), (311), (11−20), and (10−12) surface. Therefore, in total, the electronic effect is more important than geometrical one for Class I on different Rh surfaces.

(ii) For H-assisted dissociation via the CHO intermediate, as listed in Table S7, $E_{CH}{}^{TS} + E_O{}^{TS}$, $E_{CHO}{}^{IS}$, and $E_{int}{}^{TS}$ increase 1.26, 0.05, and 0.21 eV on the (100) surface, respectively. Thus, not only the electronic effect (1.21 eV) but also the geometrical effect (0.21 eV) leads to this large reduction (1.42 eV) in $E_{a,2}$ compared with the (211) surface. Moreover, the electronic effect is obviously larger than geometrical effect, which suggests that the electronic effect plays the more important role than geometrical effect. On the other Rh surfaces, such as the (111), (110), (311), (0001), (10−10), (11−20), and (10−12), the similar cases occur that the electronic effect is much stronger than the geometrical effect (see the left diagram of Figure 10b). However, on the (221) surface, although the electronic effect of 0.67 eV destabilizes the TS, the geometrical effect of 0.78 eV weakens the repulsion between CH and O and stabilizes the TS. Thus, the geometrical effect contributes to the reduction of 0.11 eV in $E_{a,2}$. In total, as shown in the left diagram of Figure 10b, the electronic effect plays the key role in H-assisted pathway through CHO on different Rh surfaces.

For H-assisted pathway through the COH intermediate, $\Delta(E_C{}^{TS} + E_{OH}{}^{TS})$ and $\Delta E_{COH}{}^{IS}$ are −1.08 and −0.37 eV, respectively, while $\Delta E_{int}{}^{TS}$ is −0.07 eV on the (100) surface, which suggests that the improved stability of the TS and the reduction of E_a are mainly determined by the electronic effect (0.71 eV). Similarly, on the (311) and (11−20) surface, the electronic effect (0.14 and 0.51 eV) is stronger than the geometrical effect (0.09 and 0.01 eV) in the change of $E_{a,2}$. However, as shown in the right diagram of Figure 10c, the reduction in $E_{a,2}$ on the (111), (0001), (10−10), and (110) surface is mainly caused by the weaken repulsion between C and OH at TS, that is, the geometrical effect. In addition, as listed in Table S7, the electronic effect (−0.80 eV) is offset by

https://dx.doi.org/10.1021/acs.jpcc.0c00909
J. Phys. Chem. C 2020, 124, 6756−6769

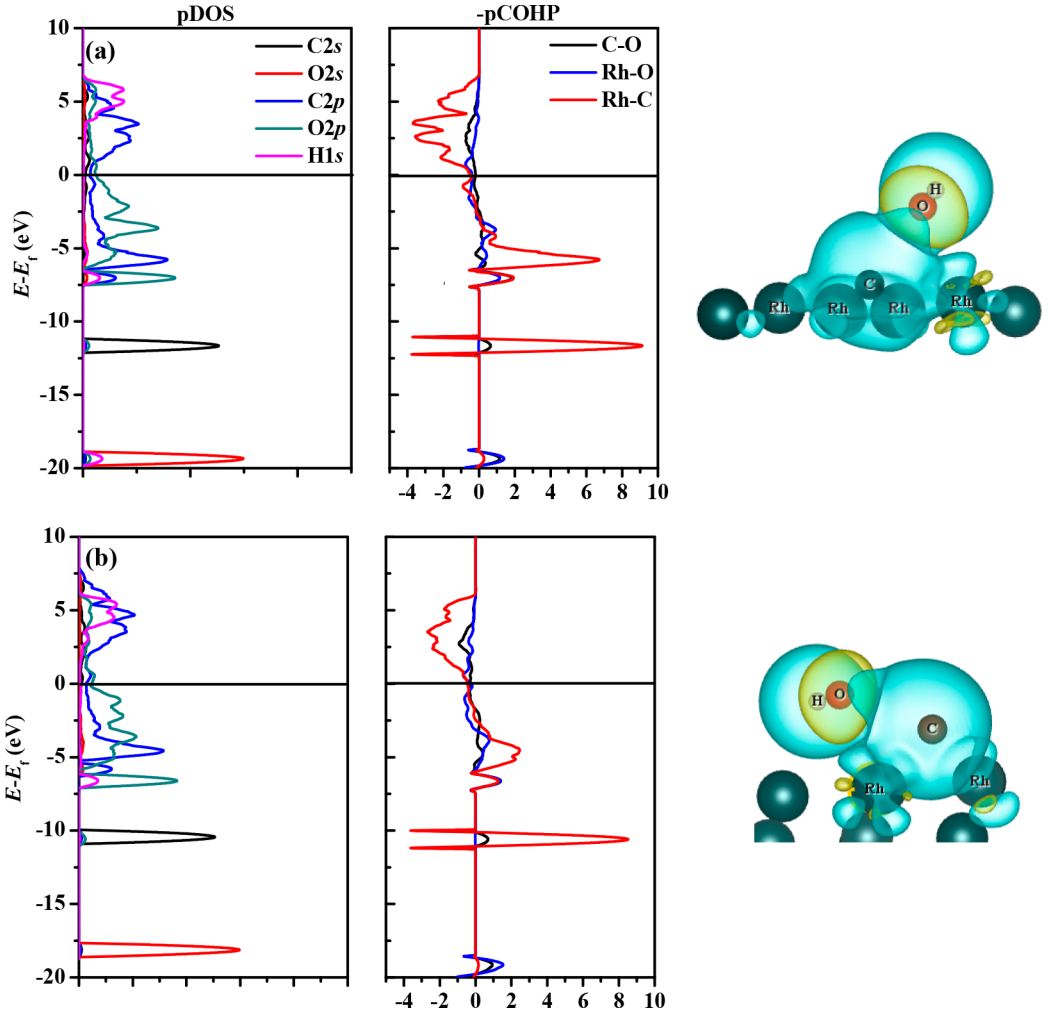

Figure 11. DOS, pCOHP curves, and differential charge density analysis for the transition state structures of COH dissociation on the (a) (100) and (b) (311) surface. The blue and yellow shaded regions represent the charge loss and charge gain, respectively. The values of the absolute isosurface are 0.01 e $Å^{-3}$.

the geometrical effect (0.81 eV) on the (10−12) surface, and thus there is no obviously change in $E_{a,2}$. Therefore, both the electronic and geometrical effect plays the key role in H-assisted dissociation via the COH intermediate on different Rh surfaces.

Based on the above analysis of Class I and II reaction, the electronic effect is the key reason influencing CO dissociation activity on Rh surfaces. The strong electronic effect stabilizes the TS structures and lowers the activation barrier for CO dissociation. Moreover, in the left areas of Figures 10a−c, the activation barrier decreases as the electronic effect becomes strong in general, which suggests that the strong electronic effect becomes benefit to CO activation; in the right areas of Figures 10a and 10c, the change of the activation barrier is in line with that of the geometrical effect, and the weaken repulsion is beneficial to CO activation.

3.6. Electronic Property Analysis. As mentioned above, the electronic effect on Rh surfaces was regarded as the dominating reason; therefore, we further analyzed the electronic property of the TSs for the most favorable pathway, H-assisted mechanism via the COH intermediate, on the most active (100) and least active (311) surface.

The pDOS and pCOHP curves for TS of COH dissociation on the (100) surface are presented in Figure 11a. According to the pDOS curves, there are two sharp peaks around −11.0 and −19.0 eV in C and O curve relative to Fermi level, which are attributed to C 2s and O 2s orbitals. The broad peak is observed at 0 to −7.0 eV, which corresponds to C 2p and O 2p orbitals hybrid with metal d-bands. In addition, combining with the pDOS and pCOHP curves, it can be found that C and O have the weak interaction in TS. The Rh−O curve presents the small peak at around −7.0 eV, and the Rh−C curve presents the sharp band at the value of −6.0 eV, which are below the Fermi level and thus occupied.

As shown in Figure 11b, on the (311) surface, it can be found that C 2s and O 2s orbitals are at the values of −10.0 and −18.0 eV, respectively,and C 2p and O 2p orbitals mixed with metal d-bands are in the range of 0 to −5.8 eV in the pDOS curve. The hybridized orbital in pDOS curve is more flat on the (311) surface compared to that on the (100) surface, which suggests that the strength of the C−O bond in TS on the (311) surface is weaker than that on the (100) surface. This accords well with the C−O distances in TSs on the (311) and (100) surfaces (2.061 vs 1.381 Å). In addition, as shown in pCOHP curves, the Rh−O curve presents the small peak at around −5.8 eV. The Rh−C curve presents the band at the value of −5.0 eV. The Rh−C interaction is

https://dx.doi.org/10.1021/acs.jpcc.0c00909
J. Phys. Chem. C 2020, 124, 6756−6769

obviously stronger than the Rh−O interaction on both (100) and (311) surfaces.

Moreover, by comparison of the pCOHP curve of the TS on the (100) with that on the (311) surface, it can be found that the Rh−C bond on the (100) is stronger than that on the (311) surface. The larger strength of the Rh−C interactions seems to be responsible for the higher stabilization of the TS, which leads to the lower E_a on the (100) compared to that on the (311) surface. The role of the M−C bond in facilitating CO dissociation was also pointed out as the reason for the increased reactivity of Co and Ni sites for CO activation on Co and Ni catalysts.[21,22]

The difference charge density analysis for TS of COH dissociation on the (100) and (311) surfaces also shows there are more electron transferring between C and Rh atom on the (100) than (311) surface, which is beneficial to stabilize the transition state structure. Thus, the difference charge density analysis accords with the pCOHP analysis. In addition, the Mulliken and Loewdin charge analyses for the transition state structures show that the C atom loses the charge of 0.58 and 0.49 *e* on the (100) surface, respectively, which is larger by 0.26 and 0.24 *e* than that on the (311) surface.

4. CONCLUSIONS

In this study, CO dissociation on different FCC and HCP Rh surfaces and crystal phases has been investigated by combining DFT with the equilibrium crystal shapes and microkinetic modeling. By comparison of the calculated overall barriers of three CO dissociation pathways on surfaces, it is found that the H-assisted pathway has lower overall activation barriers than the direct one. This suggests that H-assisted pathway is the advantageous activation way on Rh-based catalyst, which is independent of Rh crystal phases and surfaces. The microkinetic modeling show that, among different FCC and HCP Rh surfaces, the (100) surface has a relative reaction rate of 1.28×10^{11}, which is at least 10^5 times those on other surfaces. This suggests that the activity of the (100) surface is far superior to other surface. Based on the occupied ratio of the exposed surface on FCC and HCP Rh crystal shape, the CO dissociation activity of FCC Rh depends on the (100) and (111) surfaces, while that of HCP Rh depends on the (0001), (10−12), and (10−10) surfaces. The CO conversion rate on the FCC Rh is about 10^4 times that on the HCP Rh, which suggests that the FCC Rh has a higher activity than the HCP Rh. In addition, the quantitative results of the electronic and geometrical effect show that CO dissociation is primarily influenced by the electronic effect on Rh surfaces through the barrier decomposition method. The strong electronic effect was found on the most active (100) surface. The analysis of the electronic structure suggests that there is stronger electronic effect on the most active (100) than the least active (311) surface.

■ ASSOCIATED CONTENT

Supporting Information

The Supporting Information is available free of charge at https://pubs.acs.org/doi/10.1021/acs.jpcc.0c00909.

Description of the detailed microkinetic modeling method; the models of FCC and HCP Rh surfaces, the optimized IS, TS, intermediate, and FS for three CO dissociation pathways, the energy values of CO conversion rate, and the activation barrier decomposition (PDF)

■ AUTHOR INFORMATION

Corresponding Authors

Riguang Zhang − *Key Laboratory of Coal Science and Technology of Ministry of Education and Shanxi Province, Taiyuan University of Technology, Taiyuan 030024, Shanxi, P. R. China;* orcid.org/0000-0001-8956-8425; Email: zhangriguang@tyut.edu.cn

Baojun Wang − *Key Laboratory of Coal Science and Technology of Ministry of Education and Shanxi Province, Taiyuan University of Technology, Taiyuan 030024, Shanxi, P. R. China;* orcid.org/0000-0002-9069-6720; Email: wangbaojun@tyut.edu.cn, wbj@tyut.edu.cn

Authors

Xiaobin Hao − *Key Laboratory of Coal Science and Technology of Ministry of Education and Shanxi Province, Taiyuan University of Technology, Taiyuan 030024, Shanxi, P. R. China*

Lixia Ling − *Key Laboratory of Coal Science and Technology of Ministry of Education and Shanxi Province, Taiyuan University of Technology, Taiyuan 030024, Shanxi, P. R. China*

Maohong Fan − *Department of Chemical Engineering and Department of Petroleum Engineering, University of Wyoming, Laramie, Wyoming 82071, United States; School of Civil and Environmental Engineering, Georgia Institute of Technology, Atlanta, Georgia 30332, United States;* orcid.org/0000-0003-1334-7292

Debao Li − *State Key Laboratory of Coal Conversion, Institute of Coal Chemistry, Chinese Academy of Sciences, Taiyuan 030001, Shanxi, P. R. China;* orcid.org/0000-0002-6891-4787

Complete contact information is available at: https://pubs.acs.org/10.1021/acs.jpcc.0c00909

Notes

The authors declare no competing financial interest.

■ ACKNOWLEDGMENTS

This work is financially supported by the Key Projects of National Natural Science Foundation of China (21736007), the National Natural Science Foundation of China (No. 21776193, 21476155), the China Scholarship Council (201606935026), and the Top Young Innovative Talents of Shanxi.

■ REFERENCES

(1) Gupta, M.; Smith, M. L.; Spivey, J. J. Heterogeneous Catalytic Conversion of Dry Syngas to Ethanol and Higher Alcohols on Cu-Based Catalysts. *ACS Catal.* **2011**, *1*, 641−656.

(2) Yue, H. R.; Ma, X. B.; Gong, J. L. An Alternative Synthetic Approach for Efficient Catalytic Conversion of Syngas to Ethanol. *Acc. Chem. Res.* **2014**, *47*, 1483−1492.

(3) Subramani, V.; Gangwal, S. K. A Review of Recent Literature to Search for an Efficient Catalytic Process for the Conversion of Syngas to Ethanol. *Energy Fuels* **2008**, *22*, 814−839.

(4) Ao, M.; Pham, G. H.; Sunarso, J.; Tade, M. O.; Liu, S. Active Center of Catalysts for Higher Alcohol Synthesis from Syngas: A Review. *ACS Catal.* **2018**, *8*, 7025−7050.

(5) Medford, A. J.; Lausche, A. C.; Abild-Pedersen, F.; Temel, B.; Schjødt, N. C.; Nørskov, J. K.; Studt, F. Activity and Selectivity Trends in Synthesis Gas Conversion to Higher Alcohols. *Top. Catal.* **2014**, *57*, 135−142.

(6) Burch, R.; Hayes, M.J. The Preparation and Characterisation of Fe-Promoted Al_2O_3-Supported Rh Catalysts for the Selective Production of Ethanol from Syngas. *J. Catal.* **1997**, *165*, 249−261.
(7) Mei, D.; Rousseau, R.; Kathmann, S. M.; Glezakou, V. A.; Engelhard, M. H.; Jiang, W.; Wang, C.; Gerber, M. A.; White, J. F.; Stevens, D. J. Ethanol Synthesis from Syngas over Rh-Based/SiO_2 Catalysts: A Combined Experimental and Theoretical Modeling Study. *J. Catal.* **2010**, *271*, 325−342.
(8) Choi, Y. M.; Liu, P. Mechanism of Ethanol Synthesis from Syngas on Rh(111). *J. Am. Chem. Soc.* **2009**, *131*, 13054−13061.
(9) Yang, N.; Medford, A. J.; Liu, X.; Studt, F.; Bligaard, T.; Bent, S. F.; Nørskov, J. K. Intrinsic Selectivity and Structure Sensitivity of Rhodium Catalysts for C_{2+} Oxygenate Production. *J. Am. Chem. Soc.* **2016**, *138*, 3705−3714.
(10) Liu, J. X.; Li, W. X. Theoretical Study of Crystal Phase Effect in Heterogeneous Catalysis. *WIREs: Comput. Mol. Sci.* **2016**, *6*, 571−583.
(11) Bezemer, G. L.; Bitter, J. H.; Kuipers, H. P.; Oosterbeek, H.; Holewijn, J. E.; Xu, X.; Kapteijn, F.; van Dillen, A. J.; de Jong, K. P. Cobalt Particle Size Effects in the Fischer−Tropsch Reaction Studied with Carbon Nanofiber Supported Catalysts. *J. Am. Chem. Soc.* **2006**, *128*, 3956−3964.
(12) Den Breejen, J. P.; Radstake, P. B.; Bezemer, G. L.; Bitter, J. H.; Froseth, V.; Holmen, A.; De Jong, K. P. On the Origin of the Cobalt Particle Size Effects in Fischer−Tropsch Catalysis. *J. Am. Chem. Soc.* **2009**, *131*, 7197−7203.
(13) Kusada, K.; Kitagawa, H. A Route for Phase Control in Metal Nanoparticles: A Potential Strategy to Create Advanced Materials. *Adv. Mater.* **2016**, *28*, 1129−1142.
(14) Gu, J.; Guo, Y.; Jiang, Y.-Y.; Zhu, W.; Xu, Y.-S.; Zhao, Z.-Q.; Liu, J.-X.; Li, W.-X.; Jin, C.-H.; Yan, C.-H.; et al. Robust Phase Control through Hetero-Seeded Epitaxial Growth for Face-Centered Cubic Pt@Ru Nanotetrahedrons with Superior Hydrogen Electro-Oxidation Activity. *J. Phys. Chem. C* **2015**, *119*, 17697−17706.
(15) Ducreux, O.; Lynch, J.; Rebours, B.; Roy, M.; Chaumette, P. In Situ Characterisation of Cobalt Based Fischer−Tropsch Catalysts: A New Approach to the Active Phase. *Stud. Surf. Sci. Catal.* **1998**, *119*, 125−130.
(16) Kitakami, O.; Sato, H.; Shimada, Y.; Sato, F.; Tanaka, M. Size Effect on the Crystal Phase of Cobalt Fine Particles. *Phys. Rev. B: Condens. Matter Mater. Phys.* **1997**, *56*, 13849−13854.
(17) Mi, Y.; Yuan, D.; Liu, Y.; Zhang, J.; Xiao, Y. Synthesis of Hexagonal Close-Packed Nanocrystalline Nickel by a Thermal Reduction Process. *Mater. Chem. Phys.* **2005**, *89*, 359−361.
(18) Hemenger, P.; Weik, H. On the Existence of Hexagonal Nickel. *Acta Crystallogr.* **1965**, *19*, 690−691.
(19) Guo, Y.; Azmat, M. U.; Liu, X.; Ren, J.; Wang, Y.; Lu, G. Controllable Synthesis of Hexagonal Close-Packed Nickel Nanoparticles under High Nickel Concentration and Its Catalytic Properties. *J. Mater. Sci.* **2011**, *46*, 4606−4613.
(20) Kusada, K.; Kobayashi, H.; Yamamoto, T.; Matsumura, S.; Sumi, N.; Sato, K.; Nagaoka, K.; Kubota, Y.; Kitagawa, H. Discovery of Face-Centered-Cubic Ruthenium Nanoparticles: Facile Size-Controlled Synthesis Using the Chemical Reduction Method. *J. Am. Chem. Soc.* **2013**, *135*, 5493−5496.
(21) Liu, J. X.; Su, H. Y.; Sun, D. P.; Zhang, B. Y.; Li, W. X. Crystallographic Dependence of CO Activation on Cobalt Catalysts: HCP versus FCC. *J. Am. Chem. Soc.* **2013**, *135*, 16284−16287.
(22) Liu, J. X.; Zhang, B. Y.; Chen, P. P.; Su, H. Y.; Li, W. X. CO Dissociation on Face-Centered Cubic and Hexagonal Close-Packed Nickel Catalysts: A First-Principles Study. *J. Phys. Chem. C* **2016**, *120*, 24895−24903.
(23) Li, W. Z.; Liu, J. X.; Gu, J.; Zhou, W.; Yao, S. Y.; Si, R.; Guo, Y.; Su, H. Y.; Yan, C. H.; Li, W. X.; et al. Chemical Insights into the Design and Development of Face-Centered Cubic Ruthenium Catalysts for Fischer−Tropsch Synthesis. *J. Am. Chem. Soc.* **2017**, *139*, 2267−2276.
(24) Hu, J. L.; Wang, Y.; Cao, C. S.; Elliott, D. C.; Stevens, D. J.; White, J. F. Conversion of Biomass-Derived Syngas to Alcohols and C_2 Oxygenates Using Supported Rh Catalysts in a Microchannel Reactor. *Catal. Today* **2007**, *120*, 90−95.
(25) Ojeda, M.; Granados, M. L.; Rojas, S.; Terreros, P.; García-García, F. J.; Fierro, J. L. G. Manganese-Promoted Rh/Al_2O_3 for C_2 Oxygenates Synthesis from Syngas: Effect of Manganese Loading. *Appl. Catal., A* **2004**, *261*, 47−55.
(26) Huang, J. L.; Li, Z.; Duan, H. H.; Cheng, Z. Y.; Li, Y. D.; Zhu, J.; Yu, R. Formation of Hexagonal-Close Packed (HCP) Rhodium as a Size Effect. *J. Am. Chem. Soc.* **2017**, *139*, 575−578.
(27) Arakawa, H.; Fukushima, T.; Ichikawa, M.; Natsushita, S.; Takeuchi, K.; Matsuzaki, T.; Sugi, Y. Selective Synthesis of Ethanol over Rh-Ti-Fe-Ir/SiO_2 Catalyst at High Pressure Syngas Conversion. *Chem. Lett.* **1985**, *14*, 881−884.
(28) Bhasin, M. M.; Bartley, W. J.; Ellgen, P. C.; Wilson, T. P. Synthesis Gas Conversion over Supported Rhodium and Rhodium-Iron Catalysts. *J. Catal.* **1978**, *54*, 120−128.
(29) Stroppa, A.; Mittendorfer, F.; Andersen, J. N.; Parteder, G.; Allegretti, F.; Surnev, S.; Netzer, F. P. Adsorption and Dissociation of CO on Bare and Ni-Decorated Stepped Rh(553) Surfaces. *J. Phys. Chem. C* **2009**, *113*, 942−949.
(30) Zhao, X.; Zhang, R.; Wang, Q.; Li, D.; Wang, B.; Ling, L. Source and Major Species of CH_x(x = 1−3) in Acetic Acid Synthesis from Methane-Syngas on Rh Catalyst: A Theoretical Study. *RSC Adv.* **2014**, *4*, 58631−58642.
(31) Mavrikakis, M.; Bäumer, M.; Freund, H. J.; Nørskov, J. K. Structure Sensitivity of CO Dissociation on Rh Surfaces. *Catal. Lett.* **2002**, *81*, 153−156.
(32) Ma, X. F.; Su, H. Y.; Deng, H. Q.; Li, W. X. Carbon Monoxide Adsorption and Dissociation on Mn-Decorated Rh(111) and Rh(553) Surfaces: A First-Principles Study. *Catal. Today* **2011**, *160*, 228−233.
(33) Wang, J.; Liu, Z.; Zhang, R.; Wang, B. Ethanol Synthesis from Syngas on the Stepped Rh(211) Surface: Effect of Surface Structure and Composition. *J. Phys. Chem. C* **2014**, *118*, 22691−22701.
(34) Zhao, X.; Zhang, R.; Ling, L.; Wang, B. Insights into the Effect of Coverage on CO Adsorption and Dissociation over Rh(100) Surface: A Theoretical Study. *Appl. Surf. Sci.* **2014**, *320*, 681−688.
(35) Kresse, G.; Furthmüller, J. Efficient Iterative Schemes for Ab Initio Total-Energy Calculations Using a Plane-wave Basis Set. *Phys. Rev. B: Condens. Matter Mater. Phys.* **1996**, *54*, 11169−11186.
(36) Kresse, G.; Furthmüller, J. Efficiency of Ab-Initio Total Energy Calculations for Metals and Semiconductors Using a Plane-Wave Basis Set. *Comput. Mater. Sci.* **1996**, *6*, 15−50.
(37) Perdew, J. P.; Burke, K.; Ernzerhof, M. Generalized Gradient Approximation Made Simple. *Phys. Rev. Lett.* **1996**, *77*, 3865−3868.
(38) White, J. A.; Bird, D. M. Implementation of Gradient-Corrected Exchange-Correlation Potentials in Car-Parrinello Total-Energy Calculations. *Phys. Rev. B: Condens. Matter Mater. Phys.* **1994**, *50*, 4954−4957.
(39) Gajdoš, M.; Hafner, J. CO Adsorption on Cu(111) and Cu(001) Surfaces: Improving Site Preference in DFT Calculations. *Surf. Sci.* **2005**, *590*, 117−126.
(40) Wang, T.; Tian, X. X.; Li, Y. W.; Wang, J. G.; Beller, M.; Jiao, H. J. Coverage-Dependent CO Adsorption and Dissociation Mechanisms on Iron Surfaces from DFT Computations. *ACS Catal.* **2014**, *4*, 1991−2005.
(41) Liu, X.; Han, Q.; Shi, W.; Zhang, C.; Li, E.; Zhu, T. Catalytic Oxidation of Ethyl Acetate over Ru-Cu Bimetallic Catalysts: Further Insights into Reaction Mechanism via In Situ FTIR and DFT Studies. *J. Catal.* **2019**, *369*, 482−492.
(42) Tian, P.; Ding, D.; Sun, Y.; Xuan, F.; Xu, X.; Xu, J.; Han, Y. F. Theoretical Study of Size Effects on the Direct Synthesis of Hydrogen Peroxide over Palladium Catalysts. *J. Catal.* **2019**, *369*, 95−104.
(43) Yin, J.; He, Y.; Liu, X.; Zhou, X.; Huo, C. F.; Guo, W.; Peng, Q.; Yang, Y.; Jiao, H.; Li, Y. W.; et al. Visiting CH_4 Formation and C_1 + C_1 Couplings to Tune CH_4 Selectivity on Fe Surfaces. *J. Catal.* **2019**, *372*, 217−225.

https://dx.doi.org/10.1021/acs.jpcc.0c00909
J. Phys. Chem. C 2020, 124, 6756−6769

(44) Elahifard, M. R.; Jigato, M. P.; Niemantsverdriet, J. W. Direct versus Hydrogen-Assisted CO Dissociation on the Fe (100) Surface: A DFT Study. *ChemPhysChem* **2012**, *13*, 89−91.
(45) Elahifard, M. R.; Jigato, M. P.; Niemantsverdriet, J. W. Ab-Initio Calculations of the Direct and Hydrogen-Assisted Dissociation of CO on Fe(310). *Chem. Phys. Lett.* **2012**, *534*, 54−57.
(46) Hammer, B.; Hansen, L. B.; Nørskov, J. K. Improved Adsorption Energetics within Density-Functional Theory using Revised Perdew-Burke-Ernzerhof Functionals. *Phys. Rev. B: Condens. Matter Mater. Phys.* **1999**, *59*, 7413−7421.
(47) Perdew, J. P.; Burke, K.; Ernzerhof, M. Perdew, Burke, and Ernzerhof Reply. *Phys. Rev. Lett.* **1998**, *80*, 891−891.
(48) Jiang, D. E.; Carter, E. A. Adsorption and Dissociation of CO on Fe(110) from First Principles. *Surf. Sci.* **2004**, *570*, 167−177.
(49) Sheppard, D.; Xiao, P.; Chemelewski, W.; Johnson, D. D.; Henkelman, G. A Generalized Solid State Nudged Elastic Band Method. *J. Chem. Phys.* **2012**, *136*, 074103−8.
(50) Sheppard, D.; Terrell, R.; Henkelman, G. Optimization Methods for Finding Minimum Energy Paths. *J. Chem. Phys.* **2008**, *128*, 134106−10.
(51) Maintz, S.; Deringer, V. L.; Tchougréeff, A. L.; Dronskowski, R. LOBSTER: A Tool to Extract Chemical Bonding from Plane-Wave Based DFT. *J. Comput. Chem.* **2016**, *37*, 1030−1035.
(52) http://www.wxdragon.de.
(53) Wulff, G. Zur frage der Geschwindigkeit des Wachstums und der Auflösung der Krystallflächen. *Z. Kristallogr. - Cryst. Mater.* **1901**, *34*, 449−530.
(54) Zhang, W. B.; Chen, C.; Zhang, S. Y. Equilibrium Crystal Shape of Ni from First Principles. *J. Phys. Chem. C* **2013**, *117*, 21274−21280.
(55) Boettger, J. C. Nonconvergence of Surface Energies Obtained from Thin-Film Calculations. *Phys. Rev. B: Condens. Matter Mater. Phys.* **1994**, *49*, 16798−16800.
(56) Da Silva, J. L.F.; Stampfl, C.; Scheffler, M. Converged Properties of Clean Metal Surfaces by All-Electron First-Principles Calculations. *Surf. Sci.* **2006**, *600*, 703−715.
(57) Fiorentini, V.; Methfessel, M. Extracting Convergent Surface Energies from Slab Calculations. *J. Phys.: Condens. Matter* **1996**, *8*, 6525−6529.
(58) Liu, Z. P.; Hu, P. General Trends in CO Dissociation on Transition Metal Surfaces. *J. Chem. Phys.* **2001**, *114*, 8244−8247.
(59) Liu, Z. P.; Hu, P. General Trends in the Barriers of Catalytic Reactions on Transition Metal Surfaces. *J. Chem. Phys.* **2001**, *115*, 4977−4980.
(60) Liu, Z. P.; Hu, P. General Rules for Predicting Where a Catalytic Reaction Should Occur on Metal Surfaces: A Density Functional Theory Study of C-H and C-O Bond Breaking/Making on Flat, Stepped, and Kinked Metal Surfaces. *J. Chem. Phys.* **2001**, *115*, 4977−4980.

https://dx.doi.org/10.1021/acs.jpcc.0c00909
J. Phys. Chem. C 2020, 124, 6756−6769